A Three-Dimensional Radiative Transfer Model to Investigate the Solar Radiation within a Cloudy Atmosphere. Part I: Spatial Effects

WILLIAM O'HIROK AND CATHERINE GAUTIER

Institute for Computational Earth System Science and Department of Geography, University of California, Santa Barbara, Santa Barbara, California

(Manuscript received 27 September 1996, in final form 19 June 1997)

ABSTRACT

A new Monte Carlo–based three-dimensional (3D) radiative transfer model of high spectral and spatial resolution is presented. It is used to investigate the difference in broadband solar radiation absorption, top-of-the-atmosphere upwelling, and surface downwelling solar radiation in a cloudy atmosphere between 3D and 1D calculations. Spatial variations of these same radiation components (absorption, upwelling, and downwelling), together with pathlength distributions, are analyzed for different wavelengths to describe the main physical mechanisms at work.

The model contains all of the important atmospheric and surface radiative constituents. It includes Rayleigh scattering, absorption and scattering by both cloud droplets and aerosols, and absorption by the major atmospheric gases. Inputs include 3D liquid water fields, aerosols, and gas distribution, type, and concentrations.

Using satellite imagery of a tropical cloud field as input, model results demonstrate that various plane-parallel (1D) assumptions can underestimate atmospheric absorption when compared to 3D computations. This discrepancy is caused by a complex interaction of gaseous absorption, cloud droplet absorption, and the solar zenith angle. Through a sensitivity analysis, the authors demonstrate that the most important factor is the morphology of the cloud field, followed by the vertical stratification of water vapor.

1. Introduction

Clouds act as the dominant modulator of the earth's radiative energy budget and therefore are a strong interdependent link to the mechanisms driving the general circulation of the atmosphere and ocean. Although the importance of cloud–radiation interactions is well known, knowledge of their radiative properties remains a major uncertainty in the understanding and modeling of the present and future climate. While the influence of clouds on both top-of-the-atmosphere (TOA) and surface flux is directly measurable, its effect on atmospheric absorption is less clear. The prevailing view based on climate models is that the net effect of clouds on atmospheric column absorption is negligible when compared to clear skies. Yet recent global observations analyzed by Cess et al. (1995) and Cess et al. (1996), and observations in the Tropics analyzed by Ramanathan et al. (1995) and Pilewskie and Valero (1995), suggest that clouds may enhance atmospheric absorption by as much as 15–35 W m^{-2} (diurnal average) more than theory predicts.

Since the publication of Stephens and Tsay's (1990) seminal review of this phenomenon, the positive sign of the discrepancy should come as no surprise. It is rather the magnitude suggested by these recent findings that has once again stirred up a paradigmatic debate within the climate community (Wiscombe 1995). Considering that the estimates of the doubling of the greenhouse gas, CO_2, implies a 4 W m^{-2} radiative forcing on the climate system, the large discrepancy in solar absorption in the cloudy column found between theory and observations is disturbing. If the role of clouds on the radiative budget is to be fully comprehended and accurately modeled, an increased understanding of the interaction between the radiative field and both cloud microphysical and macrophysical properties is essential.

Although clouds are portrayed as being plane parallel in climate models, in nature they are far from perfectly homogeneous layers. Even stratus-type clouds can have a pronounced cellular structure, with holes (areas of low optical thickness) and heterogeneous distributions of liquid water that can modulate the radiation field to some degree (Barker and Davies 1992; Jonas 1992; Cahalan et al. 1994). Numerous studies have demonstrated that the macrophysical effects of cloud-to-cloud interactions, cloud shading, cloud leakage, and cloud radiation–water vapor interactions can greatly influence the observed albedo from the top of the atmosphere and the irradiance to the surface (McKee and Cox 1974; Aida 1977; Wendling 1977; Claußen 1982; Coakley and Davies 1986;

Corresponding author address: Dr. William O'Hirok, ICESS, University of California, Santa Barbara, Santa Barbara, CA 93106-3060. E-mail: bill@icess.ucsb.edu.

Coakley and Kobayashi 1989; Welch and Wielicki 1989; Bréon 1992; Segal and Davis 1992; Kobayashi 1993).

Fewer investigations have focused on the role of cloud macrophysics on atmospheric absorption. Davies et al. (1984) employed a 3D Monte Carlo–based radiative transfer model and simple box representations of a cloud to show that absorption is reduced by diffusion of radiation out of the cloud sides. Stephens (1988a) calculated radiative properties for cloud structures given by Gaussian and harmonic functions using Fourier transforms of the radiative transfer equation. Compared to a uniform cloud, the absorption is smaller. But Stephens (1988b) also demonstrates theoretically that the absorption can be greater depending on the inhomogeneities used in the calculations. For a towering three-dimensional cloud, Li et al. (1995) noted a small increase in absorption using a four-spectral-band Monte Carlo model. Also using a four-spectral-band Monte Carlo model, Hignett and Taylor (1996) found absorption by stratus and stratocumulus to be lower for heterogeneous clouds than for uniform clouds. Using a stochastic model, Byrne et al. (1996) demonstrated that longer pathlengths caused by broken clouds can enhance absorption. One difficulty in reconciling the differences between these results is that, while in some cases the absorption refers to that which takes place within the cloud, in other cases the absorption is for the entire atmospheric column in the presence of clouds. Furthermore, given the complexities of computing radiative transfer in three dimensions and the computer resources required, all of these approaches, to some degree, contain substantial simplifications in either spectral resolution, atmospheric composition, or cloud morphology. In this paper, we investigate the effects of cloud morphology on atmospheric absorption, using a Monte Carlo–based radiative transfer model with both high spectral and spatial resolution that contains all of the important radiative constituents of the atmosphere. The realistic cloud field representation used in this simulation has been extracted from satellite visible and infrared imagery. From analysis of the detailed spatial results, we discuss the mechanisms responsible for the absorption in a 3D cloudy atmosphere and explain the main deficiencies of 1D radiative transfer codes that depend on plane-parallel cloud assumptions. In this paper (Part I) we only address spatial effects. Spectral effects are discussed in a companion paper (O'Hirok and Gautier 1998, hereafter Part II).

2. Radiative transfer model

a. Review of previous models

The radiative transfer model used in this study is a diagnostic tool for investigating the 3D radiative field not only for clouds, but for other atmospheric constituents such as water vapor and aerosols, or surface features such as land–ocean surface feature mosaics, complex terrain, and plant canopies. In this paper, the model discussion is limited to the cloud and atmospheric components. The model is based on the Monte Carlo method, which has been frequently applied in analyzing cloud–radiative interactions as a result of the inadequacy of analytical 3D approaches. Essentially, the method is a direct simulation of the physical processes involved in radiative transfer, whereby the flow of the radiation is computed photon by photon based on a set of probability functions. These functions describe the distance a photon travels before an interaction, the result of the interaction (scattering or absorption), and the resulting scattering direction. The probabilities vary with the cloud microphysics or atmospheric constituents involved and the wavelength of the incident radiation.

Generally, clouds used in 3D simulations have consisted of simple geometric shapes or arrays composed of a constant liquid water amount confined to a single atmospheric layer. With advances in computer technology, higher-resolution cloud fields derived from stochastic modeling methods or satellite imagery have been incorporated into the models (Barker and Davies 1992; Cahalan et al. 1994; Zuev and Titov 1995; Hignett and Taylor 1996). Spectrally, computations have been made at one or, at most, a few wavelengths to represent the scattering properties for clouds over the entire solar spectrum. A review of the literature shows that molecular scattering and aerosol effects have apparently not been incorporated in any previous Monte Carlo modeling studies for cloudy atmospheres.

Accounting for cloud droplet absorption represents a relatively simple problem. Computations can be made at each photon interaction, based on the cloud droplet single scattering albedo, or during postprocessing using photon interaction statistics. Water vapor absorption represents a more formidable challenge because of its more highly variable spectral nature. One method is to infer the absorption based on the pathlength distribution statistics generated during the Monte Carlo process. Unless the water vapor field is considered homogeneous, however, the memory requirements for this method can be prohibitive for all but the most simple spatial configurations. This technique also requires the scattering parameters to be spectrally invariant for the width of each absorption band model. For a realistic atmosphere that includes molecular scattering, aerosol scattering, clouds of various droplet size distributions, and an underlying reflecting surface, the width of such a band can become quite narrow. Another approach is to compute the water vapor absorption between each scattering event by using the pathlength between the scattering locations and a transmission function that is modified by the total pathlength of the photon. Although this method can be quite accurate, it is also computationally expensive since a constant number of calculations must be performed for every photon interaction within each spectral absorption band. The method used in this research, and elaborated in the description of the design

of the model, simulates as closely as possible the physical process of a photon's interaction with water vapor by directly incorporating the effect of gas molecules into the probability functions. Computations are made at each waveband, but the number of calculations required for each interaction is dynamic and generally less than what is required in the preceding approach.

b. Design of the model

The design philosophy employed for this model is to represent the atmosphere and clouds in a manner as realistic as possible, and keep the number of theoretical assumptions and inferences to a minimum. Thus, computations are made in the most physically real sense as possible, and any reduction in computational expense comes through algorithm efficiency. In this manner, the physical processes involved in radiation transfer can be directly examined with a diminished chance of arriving at false understanding through seemingly benign assumptions or through the neglect of unforeseen interactions between the various radiative components.

The model's spatial domain consists of a cellular structure that is broken into individual homogeneous cells whose size and number depends on the complexity of the phenomena being modeled. For instance, a simulation of a sparse broken cloud field could have a large number of high-resolution cells representing the clouds and low-resolution cells portraying clear sky. Each cell contains a pointer to a database that includes all of the radiative parameters required for computing a photon's pathlength, its interaction, and scattering direction. Results, such as photon pathlength, direction, and absorption, are also stored within this database. From these data, local and domain averaged fluxes can be estimated.

All photons are initially assigned a weight ξ (see below), to represent a packet of photons. In subsequent references, one photon count is equal to a photon packet and not to the weight of the photon packet. Hence, i photon counts represents i photons of weight ξ. The distance the photon traverses between interactions within a cell, the pathlength s, is given by

$$s = -\ln(1 - R_s)/\kappa_e, \quad (1)$$

where R_s is a uniformly random distributed number within the interval [0, 1), and κ_e represents the total extinction coefficient for a given wavelength, λ. The extinction coefficient κ_e is obtained by summing the extinction coefficients for gases, molecular scattering, aerosols, and cloud droplets within a cell. If a photon escapes a cell, the part of the pathlength not used in its original cell is employed within the adjacent cell but modified to reflect the extinction coefficient of the new cell. Then, following an interaction, a new pathlength is recomputed according to Eq. (1).

For optical properties prescribed by the optical depth (τ), the volume extinction coefficient is computed by

$$\kappa_e = \tau/z_v, \quad (2)$$

where z_v is the thickness of the cell in the vertical direction. Gases include water vapor (H_2O), ozone (O_3), CO_2, N_2O, CO, CH_4, O_2, N_2, NH_3, HNO_3, NO, and SO_2. Water vapor and ozone concentrations are nominally determined from standard atmospheric profiles with modifications of the water vapor concentration based on the relative humidity within the prescribed cloud. For gaseous absorption that obeys Beer's law (i.e., self- and foreign broadening continuum), the optical depth τ_g is derived from double exponential band models (Kneizys et al. 1988).

For line absorption, a line-by-line approach is not feasible; therefore, a frequency integration approach using the k-distribution method from LOWTRAN7 is employed (Kneizys et al. 1988). For each cell, the transmission T for wavelength interval $\Delta\upsilon$ is expressed as the sum of three exponential terms

$$T_{\Delta\upsilon}(u) = e^{-k_1 u}\Delta g_1 + e^{-k_2 u}\Delta g_2 + e^{-k_3 u}\Delta g_3, \quad (3)$$

where u is the gas amount, and k_j represents the effective absorption coefficient for $T_{\Delta\upsilon}$ and is weighted by Δg_j, which sums to unity. This method allows computations to be performed independently on each term as if it were a monochromatic problem (Isaacs et al. 1987). Thus, from its entrance at the top of the atmosphere to its termination, each photon must be processed three times. For gaseous bands that overlap, this procedure will introduce some error, but in the shortwave region, the only important overlap occurs at 2.7 μm for H_2O and CO_2 (Liou 1980) where, at that wavelength, absorption within the atmosphere is already maximized.

The Rayleigh scattering optical depth τ_r and aerosol optical depth τ_a are also derived from LOWTRAN7. Aerosols within the model include boundary layer (rural, urban, and oceanic), tropospheric, and stratospheric (background stratospheric, aged volcanic, fresh volcanic, and meteor dust) types. For stratospheric aerosols, τ_a is directly specified; for the boundary layer aerosols, τ_a is computed from a specified horizontal visibility referenced at 0.55 μm and adjusted for the relative humidity and the aerosol scattering efficiency for λ. Cloud droplet optical thickness, τ_c, is a user-specified parameter and can be assigned in terms of either cloud liquid water content (LWC) or τ_c specified at 0.55 μm. When computed from LWC, it follows that

$$\tau_c = (3q\text{LWC})/(4\rho r_e), \quad (4)$$

where r_e is the effective radius of the cloud droplet distribution, q is cloud-scattering efficiency for λ, and ρ is the density of water. The surface, in the case of a solid or liquid, is treated as having an infinite optical depth.

The type of particle interaction a photon experiences within a cell is based on the ratio of a particle's optical depth, τ_i, to the total optical depth τ of a cell. A second random number, R_i, within the interval [0, 1) is generated, and a particle is selected according to R_i's location with regard to the cumulative probabilities of

each atmospheric constituent. For example, if $(\tau_1 + \tau_2)/\tau \leq R_i < (\tau_1 + \tau_2 + \tau_3)/\tau$, then the photon is deemed to have interacted with the third particle (represented by τ_3) listed in the probability table. Since the total optical depth and gaseous optical depth change with the k used in the k-distribution method, three probability tables are required per cell.

During an interaction, the energy absorbed ξ' within a cell is defined by

$$\xi' = \xi(1 - \omega_0), \tag{5}$$

where ω_0 is the single scattering albedo that describes the ratio of the scattering cross section to the extinction cross section of a gas or particle. The remaining energy $\xi\omega_0$ is scattered. Rayleigh single scattering albedo, ω_{0r}, is equal to 1. Aerosol single scattering albedo ω_{0a} is computed from a database incorporated within LOWTRAN7 and is a function of aerosol type, relative humidity of the cell, and λ. For cloud droplets, the single scattering albedo ω_{0c} is sensitive to r_e and λ, and is derived from a database produced through Mie theory calculations. For this study, the surface is treated as Lambertian, and the single scattering albedo variable for the surface, ω_{0s}, is made equivalent to the albedo of the surface.

Although gaseous absorption by definition has a single scattering albedo equal to 0, ω_{0g} is actually set to a user-defined η that remains constant for each photon processed. This method reduces the statistical variance in regions that may be surrounded by high gas concentrations (Lewis and Miller 1984). For $\eta = 0$, the gas extinction coefficient is equal to the gas absorption coefficient. If η is set >0, the gas extinction coefficient is scaled by $(1 - \eta)^{-1}$. The direction of travel by the photon is not changed after a gas interaction. When ξ becomes smaller than a predefined threshold, a random number, R_t, within the interval (0, 1) is selected. If $R_t < 0.5$ then the photon is terminated; otherwise, the photon continues with ξ being doubled (Lewis and Miller 1984). For domain averaged fluxes, the computational cost of using a high η outweighs the statistical benefits gained, and so $\eta = 0.5$ was chosen for the computations made in this study.

When a photon is scattered, the direction θ from its previous trajectory is determined from a probability function, $P_p(\theta)$, based on the normalized phase function $P(\theta)$ of the scatterer. The probability of a photon being scattered between 0 and α is given by

$$P_p(\theta) = 2\pi \int_0^{\alpha} P(\theta)\, d(\cos\theta). \tag{6}$$

By setting $P_p(\theta)$ to a new uniform random number, R_p, within the interval [0, 1), the angle α is found by solving Eq. (6) for the upper limit of the integration (McKee and Cox 1974). The azimuth angle around the direction of propagation is randomly chosen between 0 and 2π.

The phase functions are the Rayleigh scattering phase function for molecular scattering, the Henyey–Greenstein approximation for aerosols, and for clouds either the Henyey–Greenstein approximation or a direct determination of the phase function from Mie theory (Wiscombe 1980). The asymmetry factor g used in the Henyey–Greenstein approximation for aerosols is wavelength dependent and interpolated from a set of tables within LOWTRAN7. For cloud droplets, the asymmetry factor g, the size parameter x, and the refractive index m used in the Mie calculations also depend on wavelength, computed at a 0.005-μm resolution.

As mentioned above, the surface is characterized as Lambertian and is thus independent of the incident direction. The angle for a photon that is reflected from the surface, θ_r, is computed from

$$\theta_r = \cos^{-1}(R_r^{1/2}), \tag{7}$$

where R_r is a new uniform random number within the interval [0, 1) (Barker and Davies 1992). The azimuth angle is again randomly chosen between 0 and 2π.

The accuracy of the flux estimates is proportional to the square root of the number of photons used in the simulation (Cashwell and Everett 1959). For simple applications, the number of photons required is predetermined from Bernoulli probability based on estimates of the resulting flux and the desired level of random error. Since the goal of these simulations is to predict these fluxes using photons that are weighted, it is difficult (if not impossible) to estimate the number of photons required prior to the initialization of the model run (Cashwell and Everett 1959). Consequently, within this model a convergence criterion is applied, and the Monte Carlo process is terminated once a desired accuracy has been achieved. The convergence is considered to occur when the domain averages of atmospheric absorption, transmission, and reflectance, as measured as a percent of the TOA input, all change by less than a given percentage i over three consecutive intervals of j photon counts.

c. Running modes

To directly ascertain the 3D effects of the radiation field, the model can be run in three modes: the plane-parallel mode (PPM), the independent pixel approximation mode (IPM), and the three-dimensional (3DM) mode. For PPM computations, the model is composed of one single atmospheric column that is horizontally homogeneous. In the IPM, plane-parallel computations are essentially performed at each cell and a photon is constrained to a horizontally homogeneous atmospheric column. After a photon enters the top of the model, the photon remains in the same column as it traverses in the vertical direction. If the photon reaches the boundary of the column, it returns at the opposing boundary with the same trajectory, thus creating a cyclic boundary. Hence, the photon experiences variations in optical depth and atmospheric constituent microphysics only in

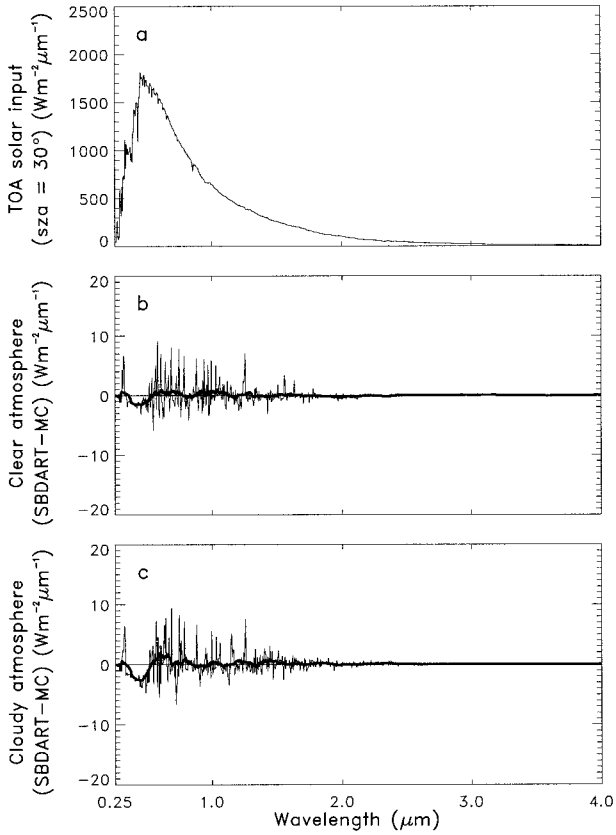

FIG. 1. Comparison of results for the Monte Carlo (MC) model and the discrete ordinates atmospheric radiative transfer model (SBDART). (a) Solar spectrum input at top of the atmosphere (TOA) for both models. (b) Difference in atmospheric absorption between MC and SBDART for clear sky conditions at a solar zenith angle = 30°. (c) Difference in atmospheric absorption between MC and SBDART for a plane-parallel cloud of optical thickness (τ = 40) and effective radius (r_e = 8 μm) at 30°. Heavy line indicates 100-nm running mean.

the vertical direction. By comparison, the photon can traverse horizontally for the 3DM computations, thereby allowing it to encounter variations in optical depth and constituent microphysics in both the horizontal and vertical directions. Only at the edges of the model do the cyclic boundaries come into effect.

d. Model comparisons

To check the validity of the atmospheric component of the model, a comparison was made with a Discrete-Ordinate Radiative Transfer model (SBDART) (Ricchiazzi et al. 1998 for clear and cloudy (plane-parallel) skies. The two models use the same transmission coefficients and much of the same input files, and therefore the results of the two models should be directly comparable. Since SBDART at the time of this comparison was limited to the Henyey–Greenstein approximation, this approximation was employed within both models for all computations. These calculations were made for both the broadband interval (0.25–4.0 μm) and, spectrally, at 0.005-μm resolution. Monte Carlo computations were made using the IPM and 3DM to determine if any biases were introduced by the cyclic conditions. For IPM and 3DM, all horizontal cells were given the same input parameters, reproducing, in effect, plane-parallel computations. No bias could be detected. The comparisons described below use 3DM computations.

TABLE 1. Total broadband (0.25–4.0 μm) differences between SBDART and Monte Carlo model for upwelling flux, downwelling flux, and atmospheric absorption for clear and cloudy sky at solar zenith angles of 0°, 30°, and 60°. Cloud optical thickness between 5 and 80 for geometric thickness ranging from 1 to 6 km.

τ	0	5	10	20	40	80
km	0	1	1	2	4	6
TOA upwelling flux (W m^{-2})						
0°	−1.60	−1.06	−0.22	1.78	1.89	1.39
30°	−1.44	−0.93	−0.47	−0.74	−0.08	−0.30
60°	0.69	−0.26	−0.24	−1.01	−0.38	−0.67
Surface downwelling flux (W m^{-2})						
0°	2.25	1.02	−0.13	−1.19	−1.45	−0.47
30°	1.57	0.89	0.16	0.56	−0.04	0.21
60°	−0.16	0.32	0.27	0.47	0.19	0.20
Atmospheric absorption (W m^{-2})						
0°	−0.60	0.09	0.36	−0.62	−0.48	−0.91
30°	−0.08	0.07	0.31	0.19	0.12	0.10
60°	−0.52	−0.05	−0.02	0.55	0.19	0.46

The results of the comparisons are presented in Fig. 1, which shows a spectral plot of atmospheric absorption for clear and cloudy skies for a standard tropical atmosphere containing oceanic aerosols with 20-km visibility overlying an ocean surface with an albedo of approximately 0.02. The cloud is 1 km thick with an optical thickness of 40 and an effective radius of 8 μm. All spectral differences are less than 10 W m^{-2} μm^{-1}. The random spikes $\approx$5 W m^{-2} μm^{-1} cannot be associated with any particular physical process and thus are believed to be noise artifacts of the Monte Carlo process. A 100-nm running mean is also plotted over the data to display any bias between the models. The negative biases $\approx$2 W m^{-2} μm^{-1}, which exist mainly in the visible spectral region, are a result of the differences in treatment of aerosols. The other slight biases $\approx$1 W m^{-2} μm^{-1} are believed to be caused by the difference in vertical discretization of the atmospheric profiles (mainly water vapor) between the two models. Since the relative humidity of the air affects the absorption properties of aerosols, it is likely that part of the aerosol biases can also be attributed to this discretization.

Broadband computations obtained by the two models are provided for top-of-the-atmosphere (100 km) upwelling flux, surface downwelling flux, and total atmospheric absorption for various cloud optical and geometrical thicknesses at solar zenith angles of 0°, 30°, and 60° (Table 1). Very little difference exists between SBDART and the Monte Carlo model, with broadband mean (standard deviation) for upwelling flux, down-

welling flux, and absorption being −0.19 (1.01), 0.34 (0.97), and −0.05 (0.41) W m^{-2}, respectively.

The small spectral differences between SBDART and the Monte Carlo model is surprising since SBDART uses discrete ordinates and the Monte Carlo model depends on stochastic techniques to solve the radiative transfer equation. For the broadband fluxes it is expected that some of the Monte Carlo noise would be canceled by spectral integration and the results would be as close as shown in Table 1. The results presented are only for irradiance, and the difference between the spectral radiances of the two models is expected to be larger. More detailed comparisons await the incorporation of the Mie phase functions into SBDART.

To test the validity of the model's 3D component, the reflectance for an isolated cubical cloud devoid of an atmosphere was computed and compared to three other independently produced Monte Carlo models (McKee and Cox 1974; Davies 1978; Bréon 1992). Computations are made for clouds with optical thickness of 4.9 and 73.5 at solar zenith angles of 0°, 30°, and 60°. The McKee and Cox (1974), Davies (1978), and Bréon (1992) models all use a phase function derived by Deirmendjian (1969) for a cumulus type cloud droplet distribution (C1). For our model, the closest equivalent phase function to the C1 distribution is computed directly from Mie theory using a cloud droplet distribution with an effective radius of 6 μm.

At 0° and 60°, the difference in reflectance for the optically thick cloud is less than 0.002 between Davies (1978), Bréon (1992), and our model (Fig. 2). At 30°, there is no statistical difference between Bréon's and our results. Davies (1978) does not report reflectance for 30°. For McKee and Cox (1974) the reflectance is consistently the lowest, with the largest discrepancies occurring for the optically thin cloud at 30° and 60°. Part of the difference may be statistical [McKee and Cox (1974) report an accuracy between 1% and 2%], but the remaining difference is unexplained. Between Bréon's (1992) and our results, the largest difference (≈0.005) in reflectance is for the optically thin cloud at 60°. Although a portion of this difference is due to statistical error, much of the discrepancy may be associated with the different phase functions being used by the two models. For the optically thicker cloud, this difference is less pronounced since increased multiple scattering tends to dampen minor differences between the phase functions. While none of these models, individually, can be considered as a benchmark for accuracy, the consistency between Davies (1978), Bréon (1992), and our model for the thick cloud, and the minor differences between Bréon (1992) and our model for the thin cloud, provides us with confidence that our model properly simulates fluxes in three dimensions.

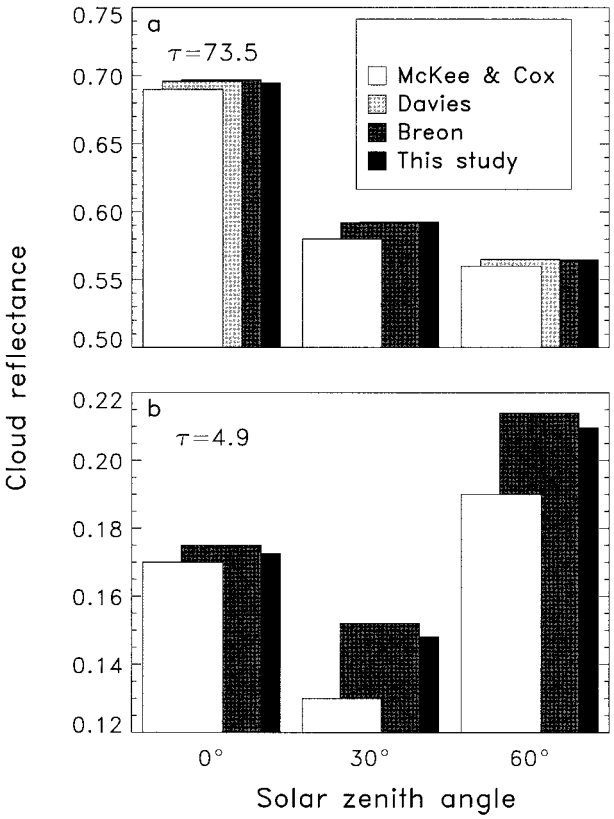

FIG. 2. Comparison among Monte Carlo models of cloud reflectance for cuboid cloud of optical thickness (a) 73.5 and (b) 4.9 at solar zenith angles of 0°, 30°, and 60°.

3. Experiment: 3D cloud absorption

To investigate the effects of 3D clouds on solar radiation, a tropical scenario was selected. Tropical clouds are strongly convective and have large vertical extent; thus any 3D effects that enhance atmospheric absorption should be most evident in this type of scenario. Tropical cloud systems are most often topped by a large anvil canopy of thick cirrus composed of ice particles and melting snow (Houze and Betts 1981). But due to the present limitations of the model, which can only handle cloud liquid water, we selected clouds that did not contain ice. Since satellite imagery is used for synthesizing the cloud field, images with cirrus anvil shields were not selected. Additionally, the shields obscure the underlying morphology that is being extracted from the satellite data. Obviously, such a choice may bias the results to cloud regimes that are most likely to experience 3D enhanced absorption. If the focus of this experiment has been to provide a definitive answer to the enhanced absorption problem globally, then such a filtering would be wholly inappropriate. The purpose of this case study, however, is to identify and explain the potential errors obtained in computing atmospheric absorption using the plane-parallel cloud assumption. If such errors do not appear in this scenario, then it would be reasonable to reject the hypothesis that the 3D effect explains enhanced absorption for all clouds.

Because GCMs use plane-parallel clouds over broad

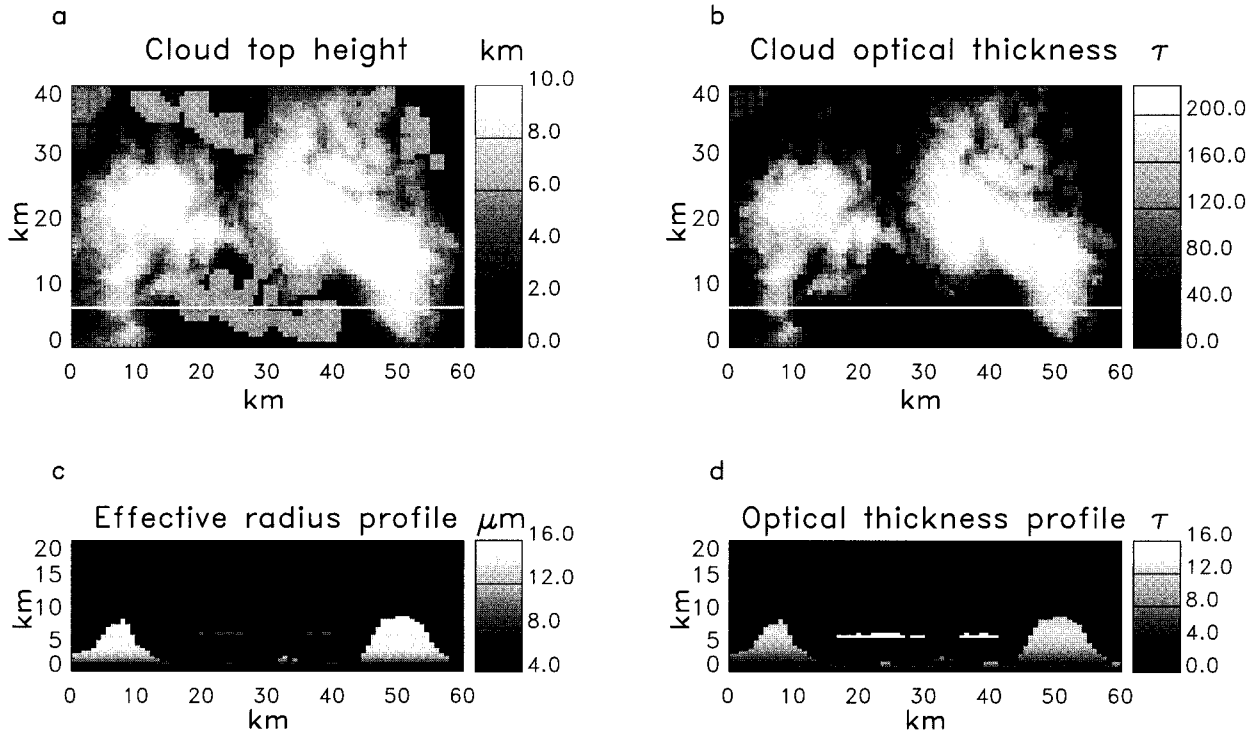

FIG. 3. Cloud model input: (a) cloud top height, (b) vertically integrated cloud column optical thickness, (c) cross section of cloud field effective radius, and (d) cross section of cloud optical thickness for 400-m-thick layers. Cross sections presented in Figs. 11, 12, and 13 are located at kilometer 6 along east–west transect as indicated by solid white lines in areal images.

spatial scales in their radiative schemes, and because the output of GCMs has been used to analyze the issue of enhanced absorption (Cess et al. 1995), differences between PPM and 3DM have been computed. A difficulty arises, however, in representing a 3D cloud field as a single homogeneous cloud layer, since any single method contains potential biases. Thus, the 3DM–PPM results should be regarded as providing a sense of the potential errors associated with the plane-parallel assumption rather than a definitive answer. Since the spatial configurations between the PPM and 3DM modes are different, the spatial mechanisms responsible for 3D effects can only be investigated using the IPM and 3DM results because both modes operate on precisely the same input fields. All 3DM and IPM computations were performed using the Monte Carlo model to reduce intermodel biases.

a. Model input

1) 3D CLOUD

Inputs to the model for 3DM and IPM consist of an artificial cloud scene embedded within a typical tropical atmosphere partitioned into 47 layers and a horizontal grid of 80 × 50 cells over an ocean surface. The albedo of the ocean varies with wavelength and, spectrally, is approximately equal to 0.02. To provide a realistic cloud scene morphology, the cloud field geometry was synthesized from cloud top heights derived from 1.1-km resolution Advanced Very High Resolution Radiometer (AVHRR) infrared images on *NOAA-14* for an area south of Hawaii. This image was rescaled both horizontally and vertically to cloud volume elements of 800 m × 800 m × 400 m, respectively (Fig. 3a). The horizontal rescaling was done to maximize the spatial resolution of the computations while minimizing discontinuities along the cloud field boundary. The cloud base altitude of the convective cells was fixed at 1200 m with a maximum cloud thickness of 8800 m. Clouds that are difficult to detect from satellite imagery because of pixel resolution or multiple cloud layering have been included to more closely resemble an actual cloud field. Numerous small cumulus congestus clouds with a maximum areal extent of 1600 m and cloud thickness of 1200 m are added near the base of the large convective cells. Scattered altostratus cloud layers 800–1200 m thick at a base altitude of 6000 m were also included, their total areal coverage being approximately 12%. The horizontal shape of the altostratus clouds was derived from a different infrared image and superimposed onto the original field. About 9% of the cloud field consists of clear skies. Within all clouds the relative humidity was raised to 95%.

Representation of the distribution of τ and r_e throughout the cloud is a difficult problem due to our limited knowledge of the internal structure of clouds. Although

TABLE 2. Plane-parallel cloud properties.

Type	Cloud base altitude (km)	Cloud top altitude (km)	Optical thickness (τ)	Effective radius (μm)
ISCCP	1.2	11.2	70	10
Stephens-Cb	2.4	6.0	404	32
Type I	3.6	7.6	102	11.7
Type II	1.2	6.4	102	11.7
Type III	1.6	6.0	102	11.7
Layer*	1.2	10.0	102	4.2–16

* Optical depth and effective radius varies by layer using the 3D large convective clouds as reference.

multifractal techniques are being developed for synthesizing liquid water distributions (Cahalan et el. 1994), their use in three dimensions remains unclear. Therefore, for this case study, generalizations about the distributions of τ and r_e have been adapted from observational studies (Bower et al. 1994). Along the horizontal plane, τ and r_e have been taken as constant within a cloud layer. Vertically, τ varies with the slope of the adiabatic curve but at an amount representing only about 5% of the saturated adiabatic liquid water content to simulate the entrainment of dry air (Fig. 3d). Although this entrainment value seems low, it was chosen to maintain the total column optical thickness within reasonable bounds. The effective radius r_e also varies vertically and ranges from 4.2 μm near the base of the convective cells to 16 μm at 2400 m above cloud base (Fig. 3c). Between 2400 m and the cloud top, r_e is held constant at 16 μm. To avoid the complexities associated with ice microphysics, the cloud is considered to be made entirely of liquid water. For the cumulus congestus clouds, r_e ranges from 4.4 to 10 μm and for altostratus clouds, from 5.5 to 8.0 μm. For the entire field the maximum optical thickness is 220, with a mean of 92 (Fig. 3b).

2) PLANE-PARALLEL CLOUD

There are numerous methods by which a 3D liquid water distribution can be portrayed as a single homogenous cloud layer, each fraught with potential biases. Therefore, rather than selecting a single plane-parallel cloud for analysis, six different types of clouds were used. These were either based on the literature or derived from combinations of the mean fields of cloud liquid water density, cloud droplet effective radius, cloud base altitude, cloud top pressure, and geometric thickness of the 3D tropical cloud field. The nomenclature used to described the mean values of the tropical cloud field are *m* (cloud median altitude), *b* (cloud base altitude), *z* (geometric thickness), *t* (cloud top pressure), r_e (effective radius), and LWC (liquid water content). The clouds used in the PPM computations are listed below. Values for these variables are provided in Table 2. All plane-parallel computations are weighted to account for the 9% clear sky.

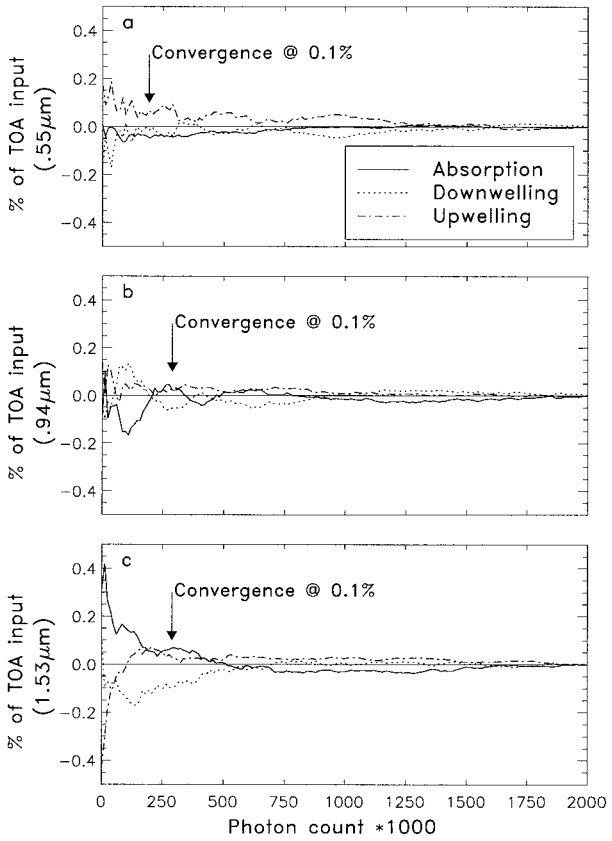

FIG. 4. Convergence of model domain averages measured as percent of top of the atmosphere input for absorption, downwelling, and upwelling fluxes at (a) 0.55-, (b) 0.94-, and (c) 1.53-μm bands. Arrows at each wavelength point to first instance when all three domain averages have changed by less than 0.1% over three consecutive intervals of 16 000 photon counts.

1) ISCCP (Fig. 9B in Rossow and Schiffer 1991).
2) Stephens-Cb (Stephens 1978).
3) Type I: cloud defined by *m*, *z*, r_e, and LWC.
4) Type II: cloud defined by *b*, *z*, r_e, and LWC.
5) Type III: cloud defined by *t*, r_e, LWC.
6) Layer: same layers as for the 3D cloud. The LWC is averaged for each layer taken over the maximum areal extent of the cloud. The r_e is not averaged.

b. Computations

Model runs were conducted for solar zenith angles between 0° and 75° at 15° increments to represent 1-h intervals for a location at the equator. The convergence criteria set for these runs was a 0.1% limit over three consecutive 16 000 photon count intervals. By testing the convergence on all three domain averages of atmospheric absorption, transmission, and reflectance rather than just one, the convergence is more stable. The stability of the convergence is demonstrated in Fig. 4 where three narrow wavebands (bandwidth = 0.005 μm) in the visible (0.55 μm), water vapor absorption

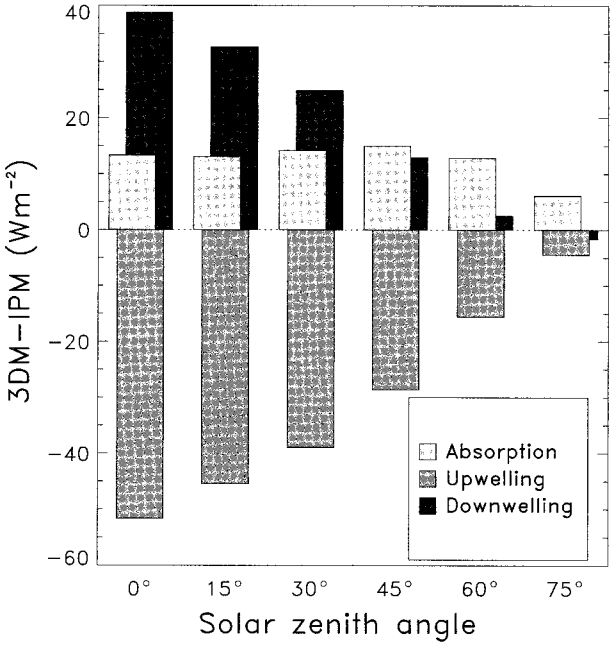

FIG. 5. Total broadband (0.25–4.0 μm) deviations of IPM from 3DM model results for atmospheric column absorption, top-of-the-atmosphere (100 km) upwelling flux, and downwelling flux at the surface.

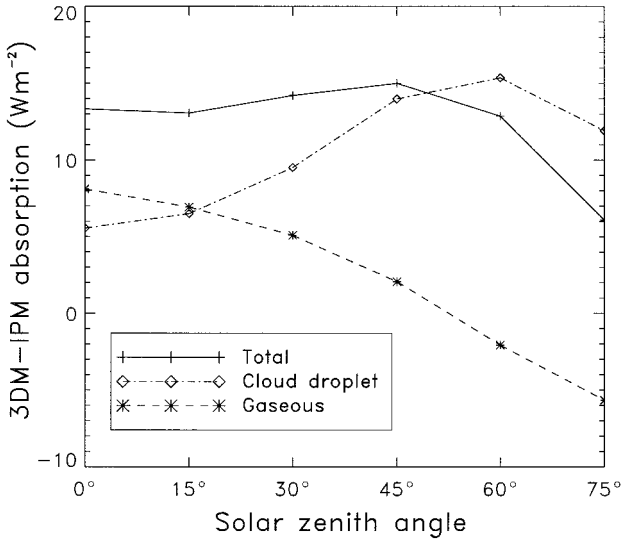

FIG. 6. Total broadband (0.25–4.0 μm) deviations of IPM from 3DM model results for atmospheric column, cloud droplet, and gaseous absorption vs solar zenith angle. Symbols represent solar zenith angles at which computations were made.

(0.94 μm), and cloud droplet absorption region (1.53 μm) were allowed to converge within 0.005%. The vertical scale in the figure represents the difference (in percentage) between the domain averages at 0.005% convergence and their values at 16 000 photon count intervals. The vertical arrow represents the points where the domain averages converge at the 0.1% criterion used in the simulations.

Computations are made for 751 wavebands representing 0.005-μm resolution between 0.25 and 4.0 μm. The number of photons required for IPM and 3DM at each solar zenith angle averages about 250 000 000. The required processing time was in the vicinity of 2500 h for a midrange Alpha processor. Computations were conducted in a parallel mode across a network of processors, so the actual length of time was on the order of a few weeks.

4. Spatial results and mechanisms

Presented in this section are broadband fluxes for the 3DM, IPM, and PPM computations for the entire spatial domain, a sensitivity analysis, and the results for two individual spectral bands (0.94 and 1.53 μm). These spectral results serve to highlight the spatial aspects of 3D radiative transfer in a cloudy atmosphere and to provide a framework for explaining the mechanisms responsible for differences between the modes. It would be desirable to present the broadband results also at a high spatial resolution, but the processing time is prohibitive at a spectral resolution of 0.005 μm. Although the number of photons processed for the two spectral bands for each mode and solar zenith angle is large (>40 000 000), the complex nature of the field cannot guarantee a good statistical sample for each cell. Thus, the spatial distributions should be viewed as being qualitative rather than providing an absolute value for a specific location.

a. Upwelling, downwelling irradiance, and absorption

By accounting for cloud morphology in the radiative transfer computations, a reduction in upwelling broadband irradiance for 3DM versus the IPM ranges from 53 W m^{-2} (or 7% in albedo), with the sun directly overhead, to 4 W m^{-2} (or 2% in albedo) at a 75° solar zenith angle (Fig. 5). Part of the reduction in the upwelling flux is associated with an increased flux at the surface. The daylight mean flux difference is 18 W m^{-2} with a 38 W m^{-2} peak at 0°. The remainder of this energy is absorbed in the atmosphere with enhanced absorption of 15 W m^{-2} at 45° and a daylight mean of 12 W m^{-2}.

A partitioning of the 3DM–IPM atmospheric absorption between absorption by gases and cloud droplets reveals a complementary relationship (Fig. 6). As the solar zenith angle increases, the difference between the 3DM and IPM due to absorption by gases decreases from 8 to −6 W m^{-2}. Concurrently, the difference as a result of absorption by cloud droplets rises from 6 W m^{-2} to a peak of 15 W m^{-2} at 60° until it drops to 12 W m^{-2} at 75°.

From the vertical profile (Fig. 7), most of the 3D enhancement takes place below 5 km when the sun is

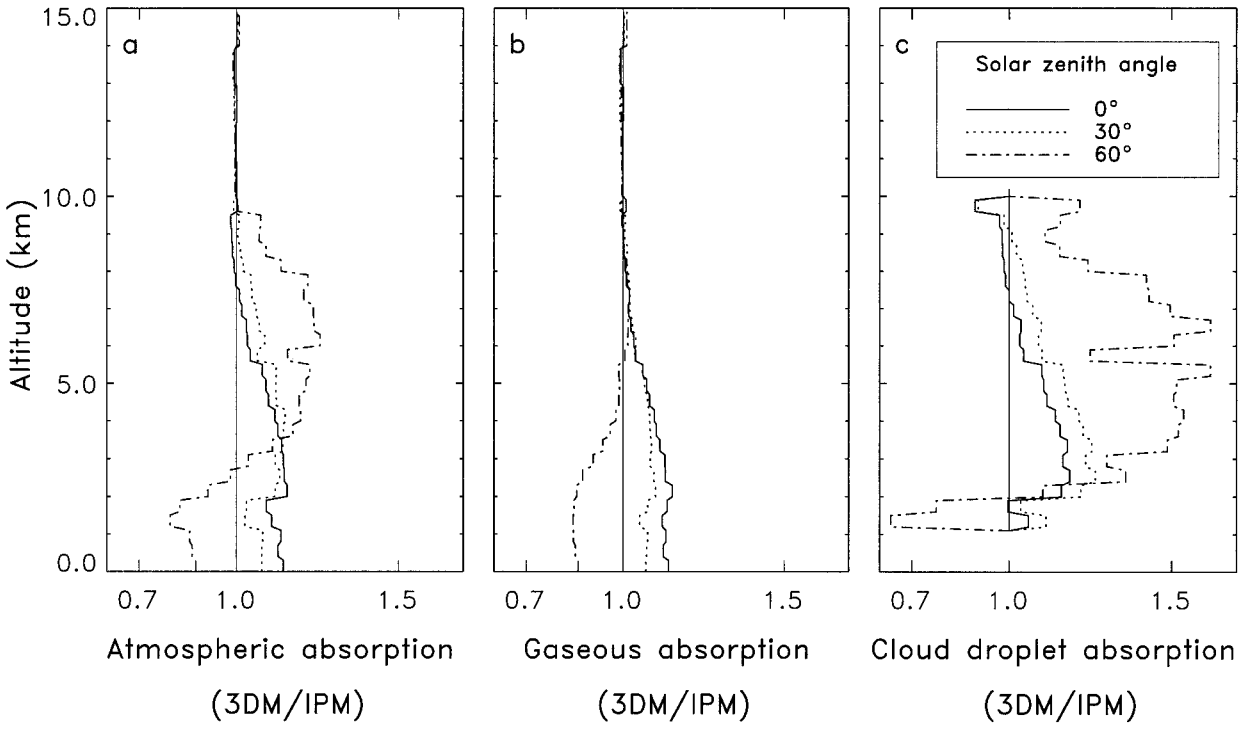

FIG. 7. Horizontally integrated total broadband (0.25–4.0 μm) ratio of 3DM to IPM model results for total atmospheric, cloud droplet, and gaseous absorption at solar zenith angles of 0°, 30°, and 60°.

directly overhead. At 30°, this altitude is raised as absorption by cloud droplets becomes more important. Some of this increase is offset by a reduction in absorption by gases (primarily water vapor) in the lower atmosphere. As the sun becomes lower in the sky at 60°, the greatest differences between the 3DM and IPM now occur high within the cloud field between 5 and 8 km. This increase in the upper portions comes at the expense of absorption by gases throughout virtually the entire atmosphere and by cloud droplets in the lowest layers of the cloud field.

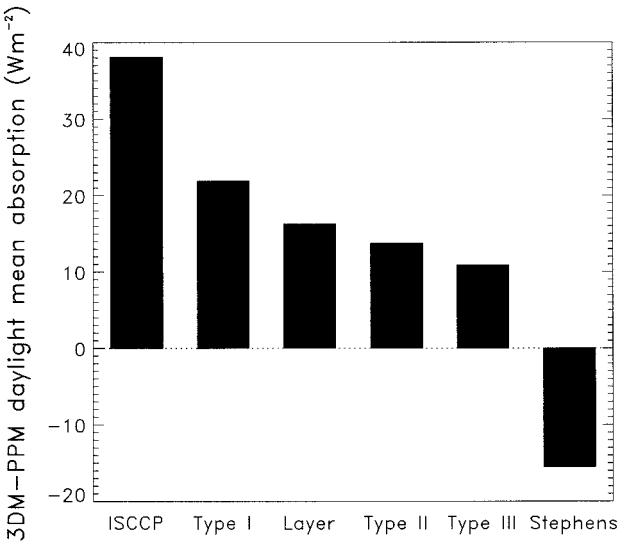

FIG. 8. Total broadband (0.25–4.0 μm) daylight mean atmospheric absorption deviations of PPM from 3DM model results for ISCCP, Stephens-Cb, Type I, Type II, Type III, and Layer plane-parallel cloud.

As previously noted, comparisons between 3D and plane-parallel clouds are provided since much of the "enhanced" absorption issue is based on the differences between observations and models that embody the plane-parallel assumption. Although the ISCCP and Stephens-Cb clouds have different optical thicknesses, effective radii, and cloud top altitudes than the 3D cloud, these cloud types are widely used in climate models and analysis and, therefore, have been included in the comparisons. As shown in Fig. 8, the difference in atmospheric absorption between the 3DM and PPM varies widely according to how the plane-parallel cloud is specified. The ISCCP and Type I clouds have the largest values with daylight mean differences of 38 and 22 W m^{-2}, respectively. These large differences are caused by high cloud top altitudes that reduce the amount of solar radiation available for gaseous absorption in the lower portions of the atmosphere. A much smaller difference of approximately 11 W m^{-2} occurs for the Type III cloud, which has a relatively low cloud top altitude, thus allowing a greater transmission of solar radiation toward the more abundant water vapor regions. The negative difference of 16 W m^{-2} for the Stephens-Cb is directly related to the lower single scattering albedo

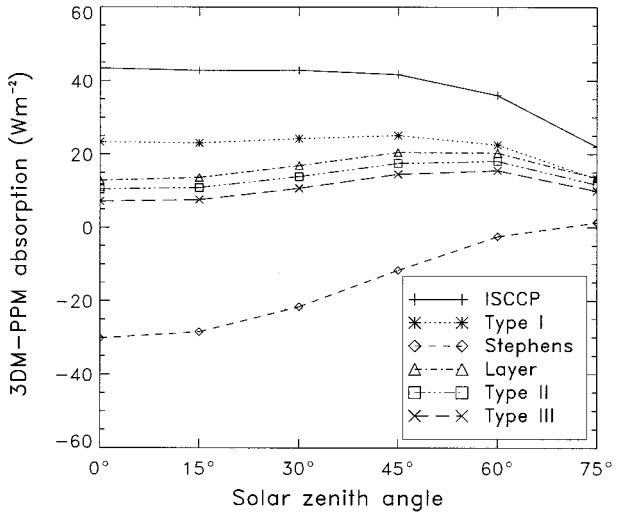

FIG. 9. Total broadband (0.25–4.0 μm) deviations of PPM from 3DM model results for ISCCP, Stephens-Cb, Type I, Type II, Type III, and Layer plane-parallel cloud vs solar zenith angle. Symbols represent solar zenith angles at which computations were made.

of the larger cloud droplets (r_e = 32 μm) prescribed for this cloud.

By plotting the 3DM–PPM absorption as a function of solar zenith angle, two curve shapes emerge (Fig. 9). For the Type II, Type III, and Layer clouds, the peak near 45° can be attributed to the complementary relationship between gaseous and cloud droplet absorption, as explained in the 3DM–IDM absorption analysis. However, for the ISCCP and Type I clouds, the curve essentially tracks the TOA radiative input, since most of the solar radiation is absorbed by the cloud or reflected back to space before it can reach the lower atmosphere, thereby negating the water vapor effects. Although the Stephens-Cb cloud top height is at an altitude lower than all the other clouds, it still exhibits a peak differential at 0°. The high optical thickness of this cloud reduces the transmission of solar radiation below the cloud top at a much higher rate than for the other clouds. Hence, the effect is the same as the ISCCP and Type I clouds, but the absolute difference in absorption is less since there are greater concentrations of gases above the cloud.

As in the case of 3DM–IPM, the 3DM–PPM shows reductions in albedo with increases in downwelling surface radiation. For the Type II cloud with the sun directly overhead, the albedo is reduced by 15% (134 W m^{-2}) with an increase of surface downwelling radiation of 124 W m^{-2}. The daylight mean enhanced atmospheric absorption is 14 W m^{-2}. The peak enhanced absorption is 18 W m^{-2} at 45°.

A dichotomy seemingly exists between these results and analysis by Ramanathan et al. (1995), where enhanced absorption appears to reduce downwelling surface radiation. However, to this point, we have only made comparisons between models and not compared models with observations. To evaluate our results within the context of observations, the constant variable should not be optical thickness, which cannot be measured directly, but cloud albedo, a value that can be quantified from satellite observations.

Assuming that the 3D computations are more representative of the radiation field in the natural world than are one-dimensional computations, plane-parallel clouds should be adjusted to match the cloud albedo obtained in the 3DM computations. Such an approach is not unique and is commonly applied in GCMs to tune model-computed liquid water content to satellite-observed albedo. The tuning can be achieved by either modifying the liquid water content of the clouds or keeping the liquid water content constant within the clouds and adjusting the amount of clear sky within the scene. By modifying the liquid water concentration within the Type II cloud, a 60% reduction in optical thickness decreased the daylight mean 3DM-''tuned'' PPM atmospheric absorption to 7 W m^{-2}. The peak 3D enhanced atmospheric absorption becomes 14 W m^{-2} for a solar zenith angle of 60°. To balance the shortwave radiative budget, the tuned PPM now shows greater downwelling radiation to the surface than the 3DM by 7 W m^{-2} averaged over the day. By increasing the clear sky in the Type II cloud scene from 9% to 23% the albedo is again matched, resulting in a 3D enhanced absorption of 17 W m^{-2} at 45° and 15 W m^{-2} for the daylight mean.

b. Sensitivity analysis

To determine the primary spatial distributions responsible for 3D enhanced absorption, a sensitivity analysis was performed at a set of wavelengths that tends to show the greatest response to this type of absorption (Fig. 10). For each analysis, one specific spatial distribution was held constant. The spatial distributions analyzed are cloud geometric and optical thickness along the horizontal plane and effective radius, cloud optical thickness, and water vapor concentration along the vertical. A reference total absorption ratio consisting of 3DM divided by IPM minus one total absorption was first computed for solar zenith angles of 0°, 30°, and 60° (Fig. 10a). This ratio is then subtracted from an absorption ratio of 3DM divided by IPM for each spatial distribution held constant (Figs. 10b–f). This measure indicates the sensitivity of the overall absorption to that particular spatial distribution. The larger the difference, the more the variation in that distribution contributes to the 3D enhanced absorption. Since each of these spatial distributions are interdependent, the effects are not expected to be cumulative.

The largest effects are caused by variations in the vertical geometry of the field (Fig. 10b). By flattening the cloud field, a large amount of the 3D enhancement effect is removed. For wavebands more sensitive to cloud droplet absorption (1.18, 1.53, and 2.10 μm), the effect is stronger with increasing solar zenith angle. On

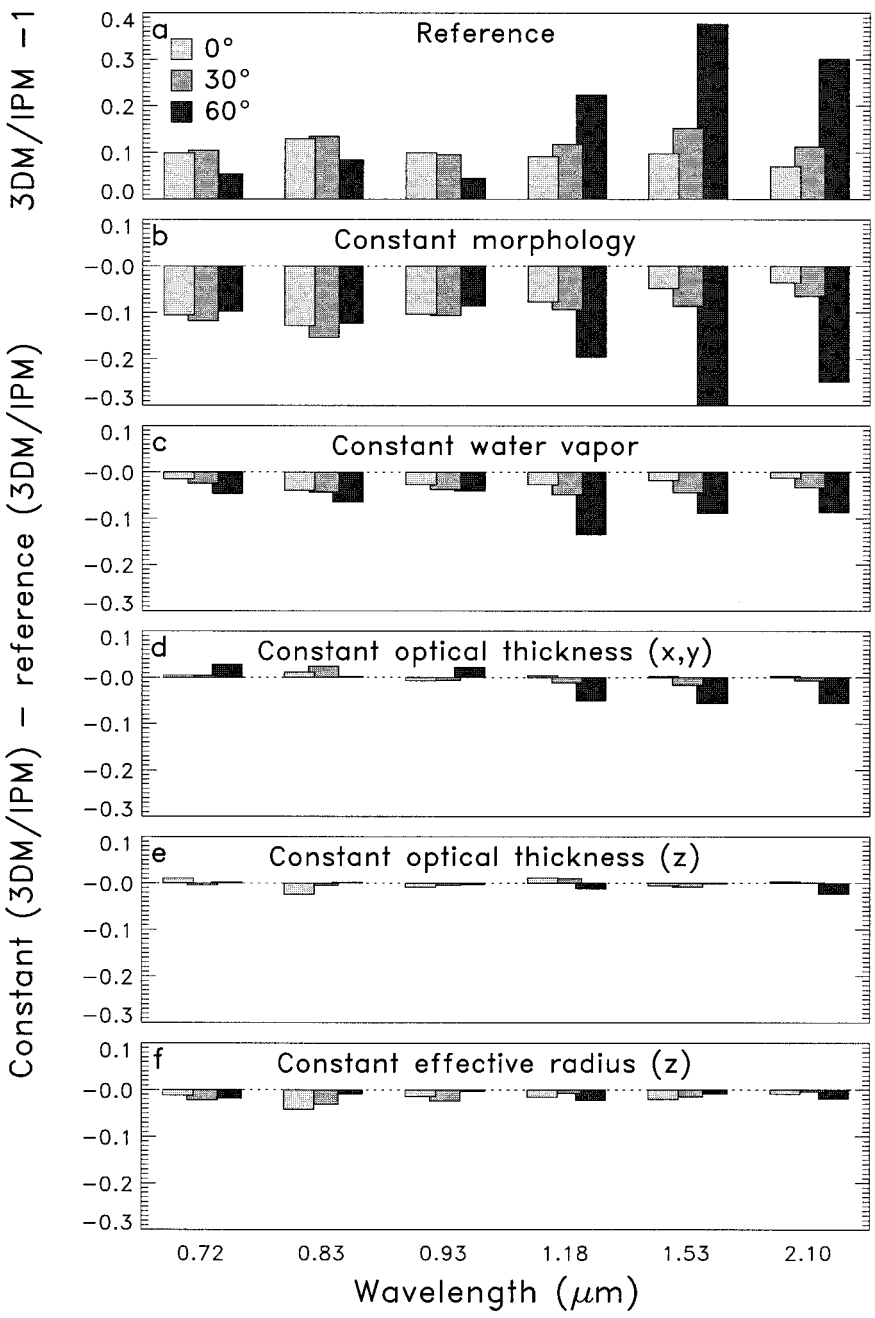

FIG. 10. Sensitivity analysis of 3D effects on atmospheric absorption at 0.72, 0.83, 0.93, 1.18, 1.53, and 2.10 μm for solar zenith angles of 0°, 30°, and 60°. (a) Reference ratio of 3DM–IPM-1. Deviations from reference when (a) morphology, (b) water vapor, (c) optical thickness in the horizontal plane, (d) optical thickness in the vertical plane, and (e) effective radius in the vertical plane are held constant.

the other hand, the water vapor wavebands (0.72, 0.83, and 0.94 μm) show greater sensitivity at lower solar zenith angles. The second largest response is obtained by holding the vertical distribution of water vapor constant (Fig. 10c). Since water vapor concentrations decrease with height and 3DM produces greater downwelling radiation, removal of this stratification reduces 3DM preferential absorption by gas. If the cloud is allowed to vary in height (Fig. 10d) but without horizontal variation in optical thickness (mean cloud optical thickness is used), there is little response for wavelengths above 1 μm except when the sun is low in the sky. Below 1 μm these variations, to a small degree, actually create negative values. A constant optical thickness in

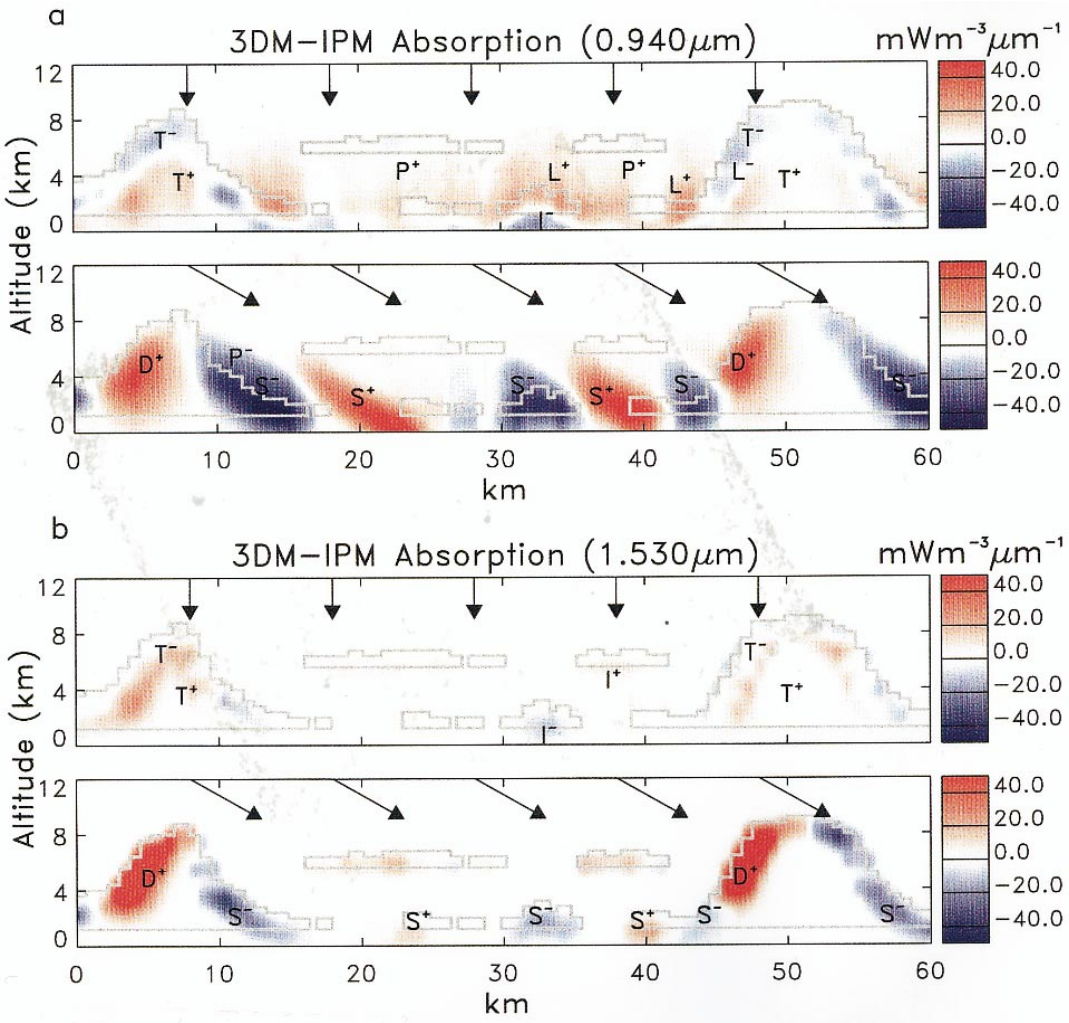

FIG. 11. Cross section along kilometer 6 east–west transect for 3DM–IPM computations. Total atmospheric absorption for (a) 0.94- and (b) 1.53-μm bands. Vertical and slanted arrows represent the direction of the solar beam at 0° and 60°, respectively. Gray line represents the profile of the cloud. Letters within the image refer to mechanisms described in the text.

the vertical direction exhibits little change in the 3D enhancement effect (Fig. 10f); a slightly greater effect is achieved when the effective radius is held constant (Fig. 10e).

c. *Spatial diagnostics*

By examining vertical cross sections of the radiative field it is possible to arrive at an explanation for some of the difference in atmospheric absorption found between plane-parallel model calculations and observations (Figs. 11, 12, and 13). The cross section to be examined is located at kilometer 6 along an east–west transect noted by the white line in Fig. 3a. Radiative fluxes are computed for the 0.94-μm band, which is highly sensitive to water vapor absorption, and the 1.53-μm band, which is dominated by cloud droplet absorption. The cross sections presented are the differences between 3DM and IPM computations for atmospheric absorption, upwelling and downwelling flux, and mean pathlength at 0° and 60° solar zenith angles. For the 1.53-μm band, only the atmospheric absorption cross section is presented since the other cross sections do not differ qualitatively from that of the 0.94-μm band. To facilitate the interpretation of these cross sections, important features have been labeled (T, L, I, S, D, P), which correspond to references made in the text. The plus and minus superscript highlight the features that either enhance or decrease the 3D absorption effect, respectively. More complex features are accompanied by schematic diagrams to elucidate the mechanisms responsible for absorption differences between 3DM and IPM (see Fig. 14). The trajectories shown in the schematics are a plausible representation of a photon's path and are not actual traces from the model.

The atmospheric absorption cross section for direct overhead sun reveals three distinct features that partially account for enhanced absorption in the 3DM (labeled

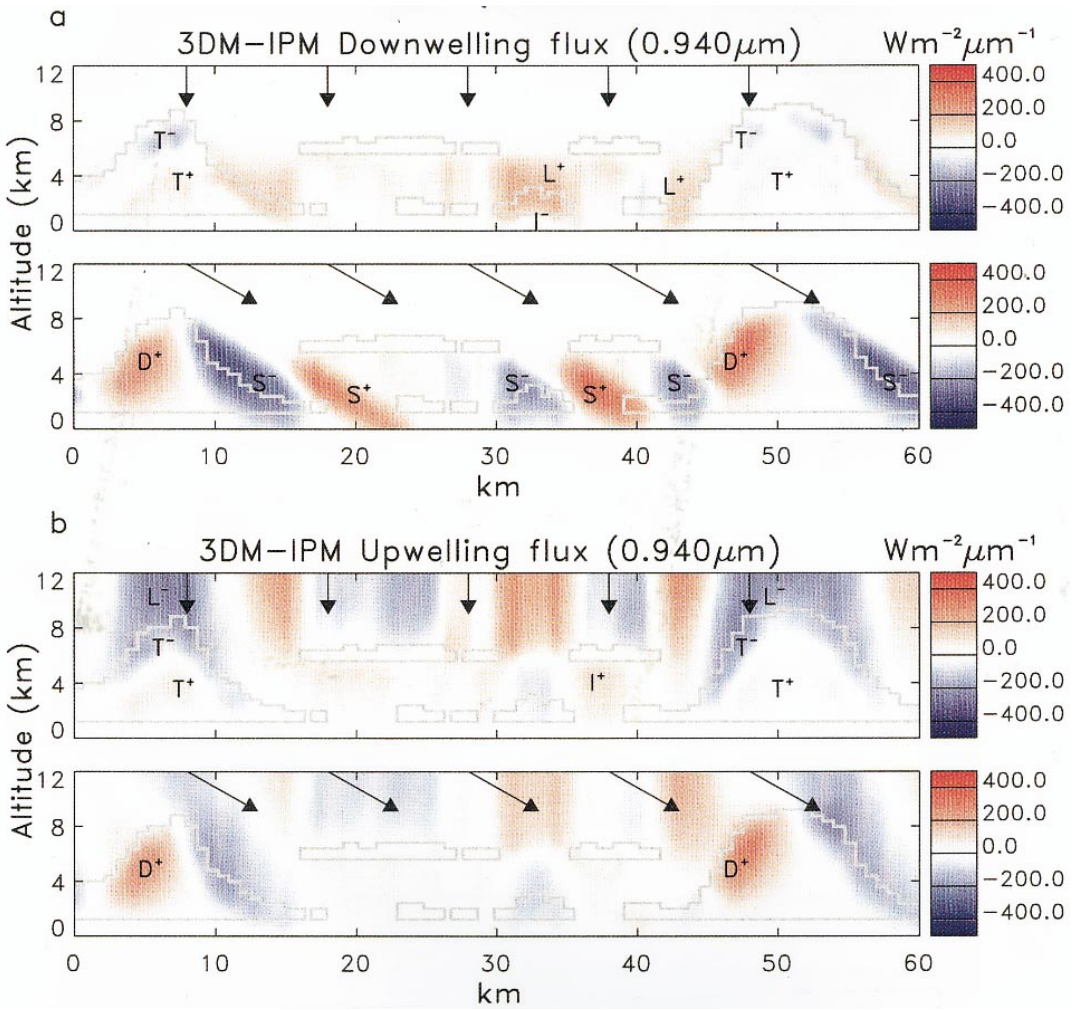

FIG. 12. Same as Fig. 11 but with (a) downwelling and (b) upwelling flux for 0.94-μm band only.

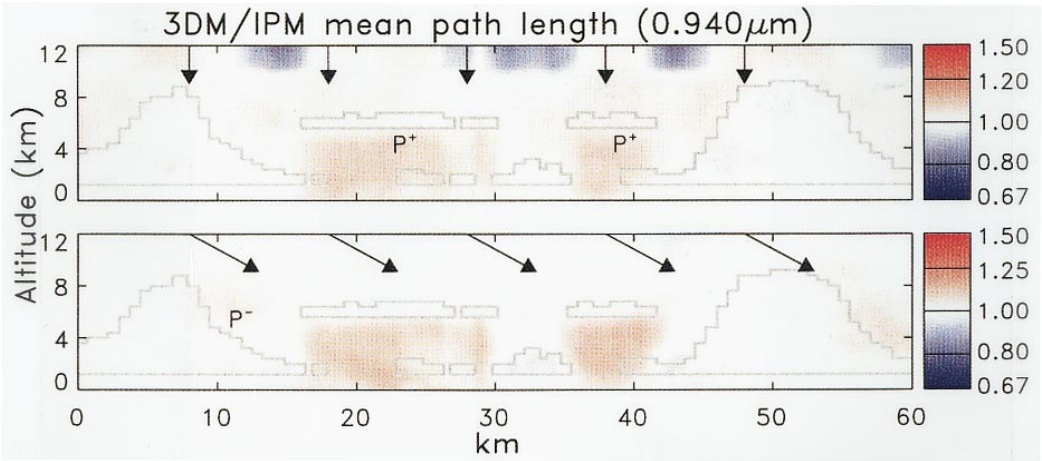

FIG. 13. Same as Fig. 11 but for 3DM–IPM ratio of mean pathlength at 0.94 μm.

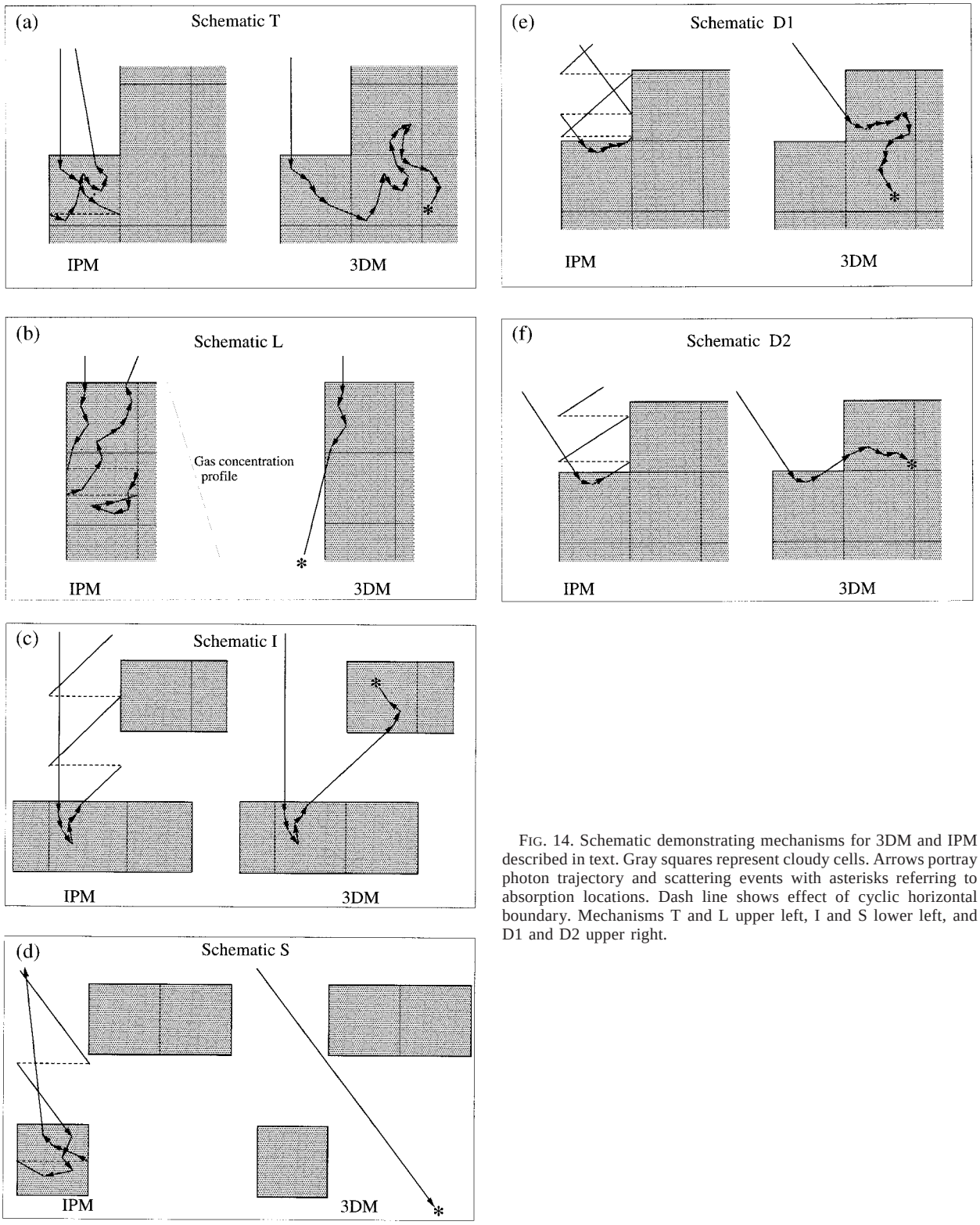

FIG. 14. Schematic demonstrating mechanisms for 3DM and IPM described in text. Gray squares represent cloudy cells. Arrows portray photon trajectory and scattering events with asterisks referring to absorption locations. Dash line shows effect of cyclic horizontal boundary. Mechanisms T and L upper left, I and S lower left, and D1 and D2 upper right.

T, L, and I on the figures). The first feature designated as T occurs for both absorption by gases and cloud droplets (Fig. 11). For the 3DM, photons are not constrained within single atmospheric columns as is the case for the IPM; therefore they reach cloud interiors more readily through horizontal transport. Once there, the photons can become trapped and eventually absorbed by gas or cloud droplets (label T^+). As indicated by the blue shading (label T^-), this increase in absorption comes at the expense of absorption near the edges of the cloud. The same pattern is observed for the downwelling and upwelling flux cross sections. The mechanism for the interior focusing/trapping in the 3DM is demonstrated in schematic T (Fig. 14a). As shown, photons in the IPM can only reach interior cells by traveling vertically within a single column. In the case of a large convective cloud, this distance can be much greater than if the photons are allowed to travel horizontally. For equal pathlengths, photons in the IPM tend be closer to the cloud top than for the 3DM and thus have a higher probability of being scattered out of the cloud. Photons in the 3DM will likely be deeper within the cloud, so the number of interactions required to escape will be greater than that for the IPM. With more interactions in the 3DM, the absorption becomes enhanced.

In addition to the reduction in 3DM flux along a cloud edge from the diffusion of photons toward the interior, much of the loss at the edge can be accounted by leakage out of the cloud. Seemingly, this loss of photons and associated reduced absorption (label L^-) should mitigate the 3D enhanced absorption effect. Whereas there is some decrease in absorption by photons escaping back toward space, the strong forward-scattering component of cloud droplets biases most of the photons toward the surface as indicated in the downwelling flux profile (label L^+) (Fig. 12a). The effect is a decrease in cloud absorption along cloud edges, but an increase in gaseous absorption from photons reaching the higher gas concentrations in the lower regions of the atmosphere. Schematic L (Fig. 14b) demonstrates how a photon in the 3DM can escape the cloud and travel toward the surface, whereas in the IPM, the horizontal boundary restriction increases the chance for a photon to be reflected back toward space. Label L^-, in the upwelling flux cross section (Fig. 12b), points to an example of this higher reflectance for the IPM. Additionally, leakage from the edges of a cloud supplement the density of photons within a clear region and produce 3D enhanced gaseous absorption (label L^+).

For a reflected photon in the IPM that has clear sky above, the photon cannot be absorbed by another cloud, unless it is scattered back toward the reflecting cloud by molecular scattering or, less likely, aerosol scattering. However, at the wavelengths where molecular scattering is significant, the ability of a cloud droplet to absorb is minimal. In the case of the 3DM, the ability for photons to travel across horizontal boundaries within the model provides a chance of interception by adjacent clouds and potential for being absorbed (label I^+). As demonstrated in schematic I (Fig. 14c), a photon in the IPM is confined to a single column and can only be scattered directly above or transmitted below a cloud, but not horizontally into another cell. Again, this difference is evident in the positive values in the upwelling flux and the 1.53-μm band absorption cross section. The horizontal confinement for IPM can, in certain instances, produce greater amounts of downwelling flux below a cloud and higher absorption below and within a cloud (label I^-) (Fig. 12a). However, the net result is for the 3DM enhanced absorption effect to dominate over the IPM, except for cases where small clouds are sufficiently isolated from one another.

As the angle of the direct solar beam steepens cloud shadowing in the 3DM reduces the amount of direct beam solar radiation reaching the lower atmosphere vis-à-vis the IPM. For the IPM, the location where the direct beam impinges is not altered by the solar angular input at the top of the atmosphere. As shown at location S^- (Fig. 11b), this is not the case for the 3DM; thus, the IPM produces more downwelling flux and greater absorption (label S^-). However, as can also be seen in schematic S (Fig. 14d) and at the point designated S^+ in the downwelling flux and absorption cross sections, there are instances of broken clouds where the direct beam can slip below a cloud and produce increased 3DM downwelling radiation and enhanced absorption.

Concurrent with a reduction in 3D atmospheric absorption by cloud shadowing is the complementary 3D enhancement of downwelling and upwelling fluxes and absorption caused by the direct solar beam impinging on the sides of a cloud (label D^+). Schematic D1 and D2 (Figs. 14e,f) shows two methods by which the strong forward-scattering characteristics of cloud droplets produces this enhancement effect. In the IPM, a photon is constrained to enter a cloud through its top. When the angle of direct beam is more closely aligned to the cloud top, a greater probability exists for the photon to be scattered and reflected back toward space. In the 3DM, a photon can enter the side of a cloud, and because of strong forward scattering the photon penetrates deeper toward the core of the cloud where the larger number of interactions required to escape increases the likelihood of absorption (schematic D1). Additionally, if a photon enters the top of the cloud and is reflected, there is a chance for the photon to enter the side of an adjoining cloud cell, again allowing for trapping and increased absorption (schematic D2).

An examination of the mean pathlength cross section (Fig. 13) provides another explanation for 3D enhanced absorption. Although a longer pathlength often suggests greater absorption, pathlength statistics are only useful when applied within a homogeneous region and convolved with the photon intensity and amount of absorber along the path. For this study, the mean pathlength refers to the average pathlength of all photons within a given cell. Thus, if one cell has photons that primarily travel

along a diagonal and a second cell has photons that dominate in the vertical direction, the first cell would have a longer mean pathlength.

Since absorption is higher for the 3DM, it may be expected that the mean pathlength is also greater. For both solar zenith angles in Fig. 13, such is the case in the atmosphere between clouds as highlighted by P^+. For the IPM, all of the photons that traverse this location are either transmitted from directly above or reflected from below the cloud. Even when the sun is not directly overhead, the tendency exists for the mean emergent angle of photons to approach the nadir direction as clouds become more optically thick (Liou 1992). Thus, at location P^+, and below most of the layered clouds, the photons entering a cell below the cloud in the IPM will have a stronger vertical component in the mean pathlength computation as compared to that for the 3DM. For the 3DM, photons arriving from directly above or below a cell will be supplemented by a strong horizontal component of the photons being scattered from the sides of clouds outside of the vertical column. For this case, the longer pathlength is associated with greater absorption.

There are occurrences when the mean pathlength for a given cell may be longer, but absorption is lower because the photon density is less. For example, at location P^- the mean pathlength is greater in 3DM, but the absorption is lower than for the IPM. As shown in the downwelling profile, this region is shaded by the cloud, leaving fewer photons available for absorption. Thus, in general, an examination of the pathlength is not sufficient to infer definitive conclusions about absorption.

5. Conclusions

We have developed a Monte Carlo–based 3D radiative transfer model of high spectral and spatial resolution that contains all of the important atmospheric radiative constituents. Comparisons with a discrete ordinates model demonstrate good agreement for both broadband and spectral computations in clear and cloudy (plane-parallel) conditions. A comparison with several other Monte Carlo models gives us confidence as to the validity of our 3D computations. Our results show that the plane-parallel assumption for clouds used in GCMs can underestimate atmospheric absorption as a result of 3D effects. The 3D enhanced absorption is primarily attributed to greater absorption by water vapor with high overhead sun and increasing cloud droplet absorption as the sun approaches the horizon. Through a sensitivity analysis, we demonstrated that the most important factor is the vertical structure of the cloud field, followed by the vertical stratification of water vapor. Internal vertical cloud inhomogeneities were found to be less important.

Using vertical cross sections of atmospheric absorption, upwelling and downwelling radiation, and mean pathlength, the mechanisms responsible for the 3D enhanced absorption have been identified and analyzed. For overhead sun, photons can penetrate deeper into clouds through focusing effects and become trapped within the cloud core. They are then absorbed by both water vapor and cloud droplets. Photons can also be scattered out of clouds to levels of the atmosphere where more water vapor is present, causing greater absorption by gases. Additionally, the 3D cloud representation provides a higher probability for photons reflected by one cloud to be intercepted by another. For higher solar zenith angles, shadowing occurs, which tends to reduce absorption by water vapor in clear sky. Concurrently, the angular direction of the solar beam causes isolated regions of high 3D enhanced absorption, as photons can enter through cloud sides and become trapped within the cloud cores. Finally, the mean pathlength is increased between clouds for the 3D case through the influence of horizontally traversing photons. However, as demonstrated, greater mean pathlength does not always entail more absorption, since it is the spatial distribution of the photons, in concert with the distribution of absorbers, that really matters.

Although previous Monte Carlo–based studies have demonstrated less or little excess absorption for 3D computations (Davies et al. 1984; Li et al. 1995; Hignett and Taylor 1996), we believe the differences between those results and ours to be more a matter of the cloud morphologies employed in the models, the boundary conditions prescribed (cyclic or noncyclic), or the absorption considered (cloud or cloudy column), rather than a disagreement on process. Since the 3D effect investigated in this study produces more absorption, it could be speculated that the plane-parallel assumption is the cause behind the issue of enhanced, ''excess,'' or ''anomalous'' absorption. Obviously, results of this simulation do not provide the complete answer, since only about a quarter of the excess absorption reported can be accounted for in the comparison between the 3D and independent pixel approximation. However, as shown, between the 3D and plane-parallel clouds the difference in daylight mean absorption ranges from -16 to $+38$ W m^{-2}. Since plane-parallel clouds are the only type presently used in climate models, perhaps a stronger emphasis should be placed on comparing results between these and 3D cloud computations. Furthermore, although the cloud field morphology used in this study tends to maximize the 3D effect, it still remains quite elementary and lacks a number of important attributes about liquid water content, cloud droplet size, and water vapor (e.g., internal 3D distributions, entrainment effects at cloud boundaries, and the effects of deep convective cloud cores) because of our limited knowledge of their 3D distributions. Additionally, ice cloud microphysics are not included and the effect of aerosols was purposely kept at a minimum. Finally, there is still no universal agreement about the magnitude of excess absorption in a cloudy atmosphere, its global distribution, or even if the phenomenon exists at all. Thus, the

quantitative discrepancies that are shown to exist in this case study do not provide a justification for rejecting the hypothesis that the 3D effect may be one of the contributing mechanisms for explaining the differences in the atmospheric absorption found between models and the real world. The appeal of this conceptual recognition is that it requires no new theory, just a better representation of clouds in climate models.

Acknowledgments. We are grateful to Dr. Paul Ricchiazzi for his valuable insight and assistance with implementation of the LOWTRAN7 routines. This research has been funded in part by Department of Energy Grants 90ER61062 and 90ER61986, and National Aeronautics and Space Administration Grant NAGW-31380.

REFERENCES

Aida, M. A., 1977: Scattering of solar radiation as a function of cloud dimension and orientation. *Quat. Spectrosc. Radiat. Transfer*, **17,** 303–310.

Barker, H. W., and J. A. Davies, 1992: Solar radiative fluxes for broken cloud fields above reflecting surfaces. *J. Atmos. Sci.,* **49,** 749–761.

Bower, K. N., T. W. Choularton, J. Latham, J. Nelson, M. B. Baker, and J. Jensen, 1994: A parameterization of warm clouds for use in atmospheric general circulation models. *J. Atmos. Sci.,* **51,** 2722–2732.

Bréon, F., 1992: Reflectance of broken cloud fields: Simulation and parameterization. *J. Atmos. Sci.,* **49,** 1221–1232.

Byrne, R. N., R. C. K. Somerville, and B. Subasilar, 1996: Broken-cloud enhancement of solar radiation absorption. *J. Atmos. Sci.,* **53,** 878–886.

Cahalan, R. F., W. Ridgway, W. J. Wiscombe, S. Gollmer, and Harshvardhan, 1994: Independent pixel and Monte Carlo estimates of stratocumulus albedo. *J. Atmos. Sci.,* **51,** 3776–3790.

Cashwell, E. D., and C. J. Everett, 1959: *A Practical Manual on the Monte Carlo Method for Random Walk Problems.* Pergamon Press, 153 pp.

Cess, R. D., and Coauthors, 1995: Absorption of solar radiation by clouds: Observations versus models. *Science,* **267,** 496–499.

——, M. H. Zhang, Y. Zhou, X. Jing, and V. Dvortsov, 1996: Absorption of solar radiation by clouds: Interpretations of satellite, surface, and aircraft measurements. *J. Geophys. Res.,* **101,** 23 299–23 309.

Claußen, M., 1982: On the radiative interaction in three-dimensional cloud fields. *Beitr. Phys. Atmos.,* **55,** 158–169.

Coakley, J. A., and R. Davies, 1986: The effect of cloud sides on reflected solar radiation as deduced from satellite observations. *J. Atmos. Sci.,* **43,** 1025–1035.

——, and T. Kobayashi, 1989: Broken cloud biases in albedo and surface insolation derived from satellite imagery data. *J. Climate,* **2,** 721–730.

Davies, R., 1978: The effect of finite geometry on the three-dimensional transfer of solar irradiance in clouds. *J. Atmos. Sci.,* **35,** 1259–1266.

——, W. L. Ridgway, and K. Kim, 1984: Spectral absorption of solar radiation in cloudy atmospheres: A 20 cm^{-1} model. *J. Atmos. Sci.,* **41,** 2126–2137.

Deirmendjian, D., 1969: *Electromagnetic Scattering on Spherical Polydispersions.* Elsevier, 290 pp.

Hignett, P., and J. P. Taylor, 1996: The radiative properties of inhomogeneous boundary layer clouds: Observations and modeling. *Quart. J. Roy. Meteor. Soc.,* **122,** 1341–1364.

Houze, R. A., and A. K. Betts, 1981: Convection in GATE. *Rev. Geophys. Space Phys.,* **19,** 541–576.

Isaacs, R. G., W. C. Wang, R. D. Worsham, and S. Goldenberg, 1987: Multiple scattering LOWTRAN and FASCODE models. *Appl. Opt.,* **26,** 1272–1281.

Jonas, P., 1992: Some effects of spatial variations of water content on the reflectance of clouds. *Ann. Geophys.,* **10,** 260–266.

Kneizys, F. X., E. P. Shettle, L. W. Abreeu, J. H. Chetwind, G. P. Anderson, W. O. Allery, J. E. A. Selby, and S. A. Clough, 1988: AFGL-TR-88-0177, Phillips Lab., Hanscom AFB, MA, 137 pp. [NTIS 206733.]

Kobayashi, T., 1993: Effects due to cloud geometry on biases in the albedo derived from radiance measurements. *J. Climate,* **6,** 120–128.

Lewis, E. E., and W. F. Miller, 1984: *Computational Methods of Neutron Transport.* John Wiley and Sons, 401 pp.

Li, Z. Q., H. W. Barker, and L. Moreau, 1995: The variable effect of clouds on atmospheric absorption of solar radiation. *Nature,* **376,** 486–490.

Liou, K. N., 1980: *An Introduction to Atmospheric Radiation.* International Geophysics Series, Vol. 25, Academic Press, 392 pp.

——, 1992: *Radiation and Cloud Processes in the Atmosphere: Theory, Observation and Modeling.* Oxford University Press, 487 pp.

McKee, T. B., and S. K. Cox, 1974: Scattering of visible radiation by finite clouds. *J. Atmos. Sci.,* **31,** 1885–1892.

O'Hirok, W., and C. Gautier, 1998: A three-dimensional radiative transfer model to investigate the solar radiation within a cloudy atmosphere. Part II: Spectral effects. *J. Atmos. Sci.,* in press.

Pilewskie, P., and F. P. J. Valero, 1995: Direct observations of excess absorption by clouds. *Science,* **267,** 1626–1629.

Ramanathan, V., B. Subasilar, G. Zhang, W. Conant, R. D. Cess, J. Kiehl, H. Grassl, and L. Shi, 1995: Warm pool heat budget and shortwave cloud forcing—A missing physics. *Science,* **267,** 499–503.

Ricchiazzi, P. J., S. Yang, C. Gautier, and D. Sowle, 1998: SBDART: A research and teaching software tool for plane-parallel radiative transfer in the earth's atmosphere. *Bull. Amer. Meteor. Soc.,* in press.

Rossow, W. B., and R. A. Schiffer, 1991: ISCCP cloud data products. *Bull. Amer. Meteor. Soc.,* **72,** 2–20.

Segal, M., and J. Davis, 1992: The impact of deep cumulus reflection on the ground-level global irradiance. *J. Appl. Meteor.,* **31,** 217–222.

Stephens, G. L., 1978: Radiation profiles in extended water clouds. Part II: Parameterization schemes. *J. Atmos. Sci.,* **35,** 2123–2132.

——, 1988a: Radiative transfer through arbitrarily shaped optical media. Part I: A general method of solution. *J. Atmos. Sci.,* **45,** 1818–1836.

——, 1988b: Radiative transfer through arbitrarily shaped optical media. Part II: Group theory and simple closures. *J. Atmos. Sci.,* **45,** 1837–1848.

——, and S. Tsay, 1990: On the cloud absorption anomaly. *Quart. J. Roy. Meteor. Soc.,* **116,** 671–704.

Welch, R. M., and B. A. Wielicki, 1989: Reflected fluxes for broken clouds over a Lambertian surface. *J. Atmos. Sci.,* **46,** 1384–1395.

Wendling, P., 1977: Albedo and reflected radiance of horizontally inhomogeneous clouds. *J. Atmos. Sci.,* **34,** 642–650.

Wiscombe, W. J., 1980: Improved Mie scattering algorithms. *Appl. Opt.,* **19,** 1505–1509.

——, 1995: Atmospheric physics: An absorbing mystery. *Nature,* **376,** 466–467.

Zuev, V. E., and G. A. Titov, 1995: Radiative transfer in cloud fields with random geometry. *J. Atmos. Sci.,* **52,** 176–190.